

## Discrete unified gas kinetic scheme for the solution of electron Boltzmann transport equation with Callaway approximation

Meng Lian<sup>1</sup>, Chuang Zhang<sup>2</sup>, Zhaoli Guo<sup>3,\*</sup> and Jing-Tao Lü<sup>1,†</sup>

<sup>1</sup>*Institute for Quantum Science and Engineering and Wuhan National High Magnetic Field Center, School of Physics, Huazhong University of Science and Technology, Wuhan 430074, China*

<sup>2</sup>*Department of Physics, Hangzhou Dianzi University, Hangzhou 310018, China*

<sup>3</sup>*Institute of Interdisciplinary Research for Mathematics and Applied Science, Huazhong University of Science and Technology, Wuhan 430074, China*



(Received 30 November 2023; accepted 10 May 2024; published 24 June 2024)

Electrons are the carriers of heat and electricity in materials and exhibit abundant transport phenomena such as ballistic, diffusive, and hydrodynamic behaviors in systems with different sizes. The electron Boltzmann transport equation (eBTE) is a reliable model for describing electron transport, but it is a challenging problem to efficiently obtain the numerical solutions of the eBTE within one unified scheme involving ballistic, hydrodynamics, and/or diffusive regimes. In this work, a discrete unified gas kinetic scheme (DUGKS) in the finite-volume framework is developed based on the eBTE with the Callaway relaxation model for electron transport. By reconstructing the distribution function at the cell interface, the processes of electron drift and scattering are coupled together within a single time step. Numerical tests demonstrate that the DUGKS can be adaptively applied to multiscale electron transport, across different regimes.

DOI: [10.1103/PhysRevE.109.065310](https://doi.org/10.1103/PhysRevE.109.065310)

### I. INTRODUCTION

With the development of nanoscience and microscale processing technologies and advancements in nanoscale temperature measurement techniques, especially the continuous miniaturization and integration of chips, the carrier transport behavior of nanosystems has become an important scientific issue in the statistical physics of nonequilibrium states [1–7]. For transport in metals and semiconductors, electrons play an important role and are characterized by rich transport phenomena, such as the thermoelectric effect [8–10], hydrodynamics [11–13], and size effects [14]. As one of the widely used methods for studying electron transport, the electron Boltzmann equation (eBTE) can be used to solve problems over a large range of scales from the nanoscale to the macroscale [15]. The Callaway approximation [16] divides the scattering processes into two types. One conserves the total crystal momenta, while the other does not. The Callaway approximation is able to successfully characterize transport behavior in the hydrodynamic regime [17,18], which has received renewed interest in recent years due to the experimental progress in graphene and other two-dimensional materials [19–21]. The development of a multiscale and high accuracy method for solving the eBTE under the Callaway approximation is highly desirable to further explore the complex characteristics of electron transport in realistic materials.

The numerical methods of the eBTE are mainly divided into two types. One uses macroscopic models to approximate

the solution, such as the drift-diffusion model and hydrodynamic equations [22–24]. These methods are simple in form, with high computational efficiency, and can accurately describe the electron transport behavior in large-scale devices. However, as the size of the device decreases, the electron mean free path becomes comparable to the characteristic length of the device. In such cases, the electron transport behavior exhibits quasiballistic or ballistic characteristics, rendering the aforementioned methods inaccurate. The other type is the direct numerical solution of the eBTE, such as the Monte Carlo (MC) method, the discrete ordinates method (DOM), and the spherical harmonic expansion (SHE) method. The MC method uses random numbers to select the scattering mechanisms and determine the drift time under external field. It is very flexible and can be combined with the actual energy band structure to analyze the complex scattering process of the carriers. Currently, MC schemes have been developed for semiconductors [25] and metals [26] but are not suitable for weak external fields due to unavoidable statistical noise; i.e., they converge slowly at small Knudsen numbers due to the decoupling of the particle drift and scattering. The DOM method discretizes both real space and wave vector space and solves the eBTE in the entire real space for each discretized wave vector [27,28]. This method is suitable for systems with high Knudsen numbers but exhibits significant numerical dissipation at small Knudsen numbers. The SHE method is widely used for the simulation of semiconductor devices [29–32]. By representing the electron distribution with spherical harmonic functions of a certain order, a series of equations which can accurately describe the transport behavior of carriers is obtained. It is more advantageous than MC in weak external fields and does not suffer from statistical noise. However, the numerical

\*zlguo@hust.edu.cn

†jtl@hust.edu.cn

results depend on the order of the expansion, which needs to be taken care of in the high-field region. Meanwhile, the high computational complexity of SHE makes it challenging to simulate high-dimensional materials, which requires the use of matrix compression techniques [33]. In addition, lattice Boltzmann methods [34] have been applied to multiscale problems in nanosystems, but they may generate nonphysical solutions at high Knudsen numbers [35].

The finite-volume discrete unified gas kinetic scheme (DUGKS), which was originally developed for multiscale gas flows [36,37], is a multiscale method with asymptotic preservation (AP) properties and was developed to address multiscale transport problems of other energy carriers. Actually, the DUGKS has been successfully applied in various fields, such as multiscale gas flow, phonon heat transfer, radiative heat transfer, and plasma transport [38]. By coupling particle drift and scattering processes simultaneously in the flux reconstruction, this scheme allows the cell size and time step to be independent of the mean free path and relaxation time and to recover adaptively from the ballistic limit to the diffusive limit. Very recently, some progress was made in electron-phonon coupled heat transfer based on the DUGKS [39]. However, it cannot be used to describe thermoelectric transport. Also, the single relaxation model used fails to capture the effects of electron momentum-conserving scattering.

In this study, we extend the application of the DUGKS to study electrical, thermal, and thermoelectric transport of electrons, incorporating the electronic band structure to iteratively solve for the temperature and chemical potential distributions. Numerical results are carefully compared to theoretical and previous numerical results. The advantage of the DUGKS in solving multiscale problems is illustrated. The rest of this paper is organized as follows: Sec. II describes the electron Boltzmann equation, Sec. III details the DUGKS for the electron Boltzmann equation, Sec. IV verifies the performance of the proposed DUGKS by simulating several typical problems, and conclusions are given in Sec. V.

## II. ELECTRON BOLTZMANN TRANSPORT EQUATION

The Boltzmann transport equation describes the evolution of the quasiparticle distribution driven by external fields applied to the system. The transport properties can be readily calculated once the distribution function is known. The eBTE is expressed as

$$\frac{\partial f}{\partial t} + \mathbf{v} \cdot \nabla_{\mathbf{r}} f + \dot{\mathbf{k}} \cdot \nabla_{\mathbf{k}} f = \left( \frac{\partial f}{\partial t} \right)_{\text{coll}}. \quad (1)$$

The distribution function  $f = f_n(\mathbf{r}, \mathbf{k}, t)$  depends on band index  $n$ , position  $\mathbf{r}$ , the wave vector  $\mathbf{k}$ , and time  $t$ . Here, we write it in an equivalent form  $f = f(\mathbf{r}, \varepsilon_n, s, t)$ , where  $\varepsilon_n$  represents the energy of the  $n$ th band (in the following, for convenience of expression, we contract the band index  $n$ ) and  $s$  represents the unit solid angle. For the three-dimensional (3D) case,  $s = (\cos \theta, \sin \theta \cos \varphi, \sin \theta \sin \varphi)$ , where  $\theta$  and  $\varphi$  are the polar and azimuthal angles. In the two-dimensional (2D) case, only  $\varphi$  is needed,  $s = (\cos \varphi, \sin \varphi)$ . The group velocity of electrons depends on the band structure and is given by  $\mathbf{v} = \nabla_{\mathbf{k}} \varepsilon_n(\mathbf{k})/\hbar$ , where  $\hbar$  is the reduced Planck constant. The electric field  $\mathbf{E}$  determines the time derivative  $\dot{\mathbf{k}} = -e\mathbf{E}/\hbar$ ,

where  $e$  is the elemental charge. The right-hand side presents the change of the distribution function due to electron collisions. It depends on the specific scattering mechanism, which can be expressed as

$$\left( \frac{\partial f}{\partial t} \right)_{\text{coll}} = - \int \frac{d\mathbf{k}'}{(2\pi)^3} \{ W(\mathbf{r}, \mathbf{k}, \mathbf{k}') f(\mathbf{k}) [1 - f(\mathbf{k}')] - W(\mathbf{k}', \mathbf{k}) f(\mathbf{k}') [1 - f(\mathbf{k})] \}, \quad (2)$$

where  $W(\mathbf{k}, \mathbf{k}')$  is the scattering kernel, which describes the rate of electron transition from state  $\mathbf{k}$  to  $\mathbf{k}'$  and is usually obtained with Fermi's golden rule.

The Boltzmann equation is a complicated nonlinear integral-differential equation which is difficult to solve even numerically. In this paper, we adopt the simplified Callaway approximation to describe the collision term, which is divided into two types, representing normal and umklapp processes. The former fulfills crystal momentum conservation, while the latter does not due to the involved extra reciprocal lattice vector. A rich set of transport phenomena can be obtained from this simplified approximation, including ballistic, diffusive and hydrodynamic regimes.

Generally, the electric potential  $\varphi$  and the electric field  $\mathbf{E} = -\nabla\varphi$  need to be obtained by solving Poisson's equation. However, when the external field is relatively weak, the electric field can be represented by the gradient of the electrochemical potential, i.e.,  $\nabla\mu \approx -e\nabla\varphi$ . We use this approximation and avoid solving the Poisson equation [17,18,40]. Appendix A contains further discussion of this approximation. The resulting eBTE can be written as

$$\frac{\partial f}{\partial t} + \mathbf{v} \cdot \nabla_{\mathbf{r}} f = \frac{f_0^U(T^U, \mu^U) - f}{\tau^U} + \frac{f_0^N(T^N, \mu^N, \mathbf{u}) - f}{\tau^N}. \quad (3)$$

Here,  $\tau^U$  and  $\tau^N$  are the relaxation times of the umklapp process and normal process, respectively, and both depend on the electron state. The Fermi-Dirac distribution  $f_0^U$  and the shifted Fermi-Dirac distribution  $f_0^N$  with a common drift velocity  $\mathbf{u}$  for all electrons are given by

$$f_0^U = \frac{1}{\exp[(\varepsilon - \mu^U)/k_B T^U] + 1}, \quad (4)$$

$$f_0^N = \frac{1}{\exp[(\varepsilon - \mu^N - \mathbf{p} \cdot \mathbf{u})/k_B T^N] + 1}, \quad (5)$$

where  $\mathbf{p} = \hbar\mathbf{k}$  is the electron momentum and  $k_B$  is the Boltzmann constant. The two sets of parameters  $\{\mu^U, T^U\}$  and  $\{\mu^N, T^N, \mathbf{u}\}$  in  $f_0^U$  and  $f_0^N$  are Lagrange multipliers in the maximum entropy principle and are responsible for the conservation of the particle number and energy in umklapp processes and the conservation of the particle number, energy, and momentum in normal processes. They are determined by the following equations:

$$\int_{\Omega_d} \int_{-\infty}^{+\infty} \boldsymbol{\psi}^U \frac{D(\varepsilon)}{\Omega_d} \frac{f_0^U(T^U, \mu^U) - f}{\tau^U(\varepsilon)} d\varepsilon d\Omega = \mathbf{0}, \quad (6)$$

$$\int_{\Omega_d} \int_{-\infty}^{+\infty} \boldsymbol{\psi}^N \frac{D(\varepsilon)}{\Omega_d} \frac{f_0^N(T^N, \mu^N, \mathbf{u}^N) - f}{\tau^N(\varepsilon)} d\varepsilon d\Omega = \mathbf{0}, \quad (7)$$

where  $\boldsymbol{\psi}^U = (1, \varepsilon)^T$  and  $\boldsymbol{\psi}^N = (1, \varepsilon, \mathbf{p})^T$  denote the conserved quantities of the umklapp process and normal process,

respectively,  $D(\varepsilon)$  is the electronic density of states, and  $d\Omega$  is the differential of the solid angle.  $\Omega_d$  is a quantity related to the dimension  $d$ . For the 3D case, i.e.,  $d = 3$ , we have  $\Omega_d = 4\pi$ ; for  $d = 2$ , we have  $\Omega_d = 2\pi$ . These equations can be used to get  $\{\mu^U, T^U\}$  and  $\{\mu^N, T^N, \mathbf{u}\}$ , once the nonequilibrium distribution function  $f$  is obtained.

The temporal parameters  $T^U$ ,  $T^N$ ,  $\mu^U$ , and  $\mu^N$  with dimensions of the temperature and chemical potential can be different from the physical ones. On the other hand, the corresponding physical quantities  $\tilde{T}$  and  $\tilde{\mu}$  are determined from the local conservation laws,

$$\int_{-\infty}^{+\infty} \int_{\Omega_d} \frac{D(\varepsilon)}{\Omega_d} f_0 d\Omega d\varepsilon = \int_{-\infty}^{+\infty} \int_{\Omega_d} \frac{D(\varepsilon)}{\Omega_d} f d\Omega d\varepsilon, \quad (8)$$

$$\int_{-\infty}^{+\infty} \int_{\Omega_d} \varepsilon \frac{D(\varepsilon)}{\Omega_d} f_0 d\Omega d\varepsilon = \int_{-\infty}^{+\infty} \int_{\Omega_d} \varepsilon \frac{D(\varepsilon)}{\Omega_d} f d\Omega d\varepsilon, \quad (9)$$

where  $f_0 = f_0(\tilde{T}_{loc}, \tilde{\mu}_{loc})$ . It can be seen that the distribution function  $f$  reduces to  $f^U$  and  $f^N$  in the diffusive and hydrodynamic regimes, respectively, while the intermediate regime it is a weighted average of the two. If  $\tau$  is constant,  $\tilde{T}$  and  $\tilde{\mu}$  calculated in the diffusive and hydrodynamic regions are the same as the spurious variables.

### III. THE DISCRETE UNIFIED GAS KINETIC SCHEME

We introduce the DUGKS for solving Eq. (3) numerically. To facilitate the solution, we rewrite Eq. (3) with discrete angular space as

$$\frac{\partial f(\mathbf{r}, \varepsilon, \mathbf{s}_\alpha, t)}{\partial t} + \mathbf{v} \cdot \nabla_{\mathbf{r}} f(\mathbf{r}, \varepsilon, \mathbf{s}_\alpha, t) = \frac{f_0 - f(\mathbf{r}, \varepsilon, \mathbf{s}_\alpha, t)}{\tau}, \quad (10)$$

where  $f_0 = (\tau^N f_0^U + \tau^U f_0^N) / (\tau^N + \tau^U)$  and  $\tau = \tau^U \tau^N / (\tau^U + \tau^N)$ . In order to accurately evaluate the zeroth-order to second-order moments of the distribution function, the discrete angle  $\mathbf{s}_\alpha$  needs to satisfy the following requirements:

$$\sum_{\alpha} w_{\alpha} = \Omega_d, \quad \sum_{\alpha} w_{\alpha} \mathbf{s}_{\alpha} = \mathbf{0}, \quad \sum_{\alpha} w_{\alpha} \mathbf{s}_{\alpha} \mathbf{s}_{\alpha} = \frac{\Omega_d}{d} \mathbf{I}, \quad (11)$$

where  $w_{\alpha}$  is the weight of the angular discretization and  $\mathbf{I}$  is the corresponding unit matrix.

Like for the calculation of the phonon Boltzmann transport equation, we use the trapezoidal integration rule to discretize the energy space. For the solid angle space, the conventional  $S_N$  quadrature is not accurate enough for large Knudsen numbers and may have a serious ‘‘ray effect.’’ To overcome these difficulties, we choose the Gauss-Legendre (GL) rule to discretize the solid angle. The real space is discretized using the finite-volume method, the midpoint rule is used for the time integration of the advection term, and the trapezoidal rule is used for the collision term. With these considerations, Eq. (10) is discretized as

$$\begin{aligned} f_{\alpha, \varepsilon, i}^{n+1} - f_{\alpha, \varepsilon, i}^n + \frac{\Delta t}{V_i} \mathbf{F}_{\alpha, \varepsilon, i}^{n+1/2} \\ = \frac{\Delta t}{2} \left[ \frac{f_{0, \varepsilon, i}^{n+1} - f_{\alpha, \varepsilon, i}^{n+1}}{\tau_{\varepsilon}} + \frac{f_{0, \varepsilon, i}^n - f_{\alpha, \varepsilon, i}^n}{\tau_{\varepsilon}} \right], \end{aligned} \quad (12)$$

where  $f_{\alpha, \varepsilon, i}^n$  denotes the cell-averaged occupation probability of electrons moving along the  $\mathbf{s}_{\alpha}$  direction in cell  $i$  at energy level  $\varepsilon$  at time  $t = n\Delta t$ ,  $V_i$  is the volume of cell  $i$ , and  $\mathbf{F}_{\alpha, \varepsilon, i}^{n+1/2}$  is the flux across the interfaces of cell  $i$ , expressed as

$$\mathbf{F}_{\alpha, \varepsilon, i}^{n+1/2} = \sum_{j \in \mathcal{N}_i} (\mathbf{v}_{\alpha, \varepsilon} \cdot \mathbf{n}_{ij}) f_{\alpha, \varepsilon}^{n+1/2}(\mathbf{x}_{ij}) S_{ij}, \quad (13)$$

where  $\mathcal{N}_i$  denotes the set of cells adjacent to cell  $i$ ,  $\mathbf{n}_{ij}$  is the unit normal vector pointing from cell  $i$  to cell  $j$ ,  $S_{ij}$  is the area of the interface  $ij$  between cells  $i$  and  $j$ , and  $f_{\alpha, \varepsilon}^{n+1/2}(\mathbf{x}_{ij})$  denotes the distribution function at the interface at time  $t_{n+1/2} = t_n + \Delta t/2$ . Two new distribution functions are introduced to remove the implicitness of Eq. (12):

$$\tilde{f}_{\alpha, \varepsilon, i}^n = f_{\alpha, \varepsilon, i}^n - \frac{\Delta t}{2} \left( \frac{f_{0, \varepsilon, i}^n - f_{\alpha, \varepsilon, i}^n}{\tau_{\varepsilon}} \right), \quad (14)$$

$$\tilde{f}_{\alpha, \varepsilon, i}^{+,n} = f_{\alpha, \varepsilon, i}^n + \frac{\Delta t}{2} \left( \frac{f_{0, \varepsilon, i}^n - f_{\alpha, \varepsilon, i}^n}{\tau_{\varepsilon}} \right). \quad (15)$$

Then, Eq. (12) can be rewritten as

$$\tilde{f}_{\alpha, \varepsilon, i}^{n+1} = \tilde{f}_{\alpha, \varepsilon, i}^{+,n} - \frac{\Delta t}{V_i} \mathbf{F}_{\alpha, \varepsilon, i}^{n+1/2}. \quad (16)$$

We can track the evolution of the distribution function  $\tilde{f}$  following Eq. (16), where the interface distribution function  $f_{ij}^{n+1/2}$  at half-time steps is reconstructed based on the eBTE, which is the key difference between the present DUGKS and classical DOM using certain direct numerical interpolations. First, along the characteristic lines of Eq. (3) from time  $t_n$  to  $t_{n+1/2}$ , the end point  $\mathbf{x}_{ij}$  is at the center of the interface between cell  $i$  and cell  $j$ :

$$\begin{aligned} f_{\alpha, \varepsilon}^{n+1/2}(\mathbf{x}_{ij}) - f_{\alpha, \varepsilon}^n(\mathbf{x}'_{ij}) = \frac{\Delta t}{4} \left[ \frac{f_{0, \varepsilon}^{n+1/2}(\mathbf{x}_{ij}) - f_{\alpha, \varepsilon}^{n+1/2}(\mathbf{x}_{ij})}{\tau_{\varepsilon}} \right. \\ \left. + \frac{f_{0, \varepsilon}^n(\mathbf{x}'_{ij}) - f_{\alpha, \varepsilon}^n(\mathbf{x}'_{ij})}{\tau_{\varepsilon}} \right], \end{aligned} \quad (17)$$

where  $\mathbf{x}'_{ij} = \mathbf{x}_{ij} - \mathbf{v}\Delta t/2$ . Again introducing two auxiliary distribution functions to remove the implicitness of Eq. (17),

$$\tilde{f}_{\alpha, \varepsilon, i}^n = f_{\alpha, \varepsilon, i}^n - \frac{\Delta t}{4} \left( \frac{f_{0, \varepsilon, i}^n - f_{\alpha, \varepsilon, i}^n}{\tau_{\varepsilon}} \right), \quad (18)$$

$$\tilde{f}_{\alpha, \varepsilon, i}^{+,n} = f_{\alpha, \varepsilon, i}^n + \frac{\Delta t}{4} \left( \frac{f_{0, \varepsilon, i}^n - f_{\alpha, \varepsilon, i}^n}{\tau_{\varepsilon}} \right), \quad (19)$$

then the Eq. (17) can be expressed as

$$\tilde{f}_{\alpha, \varepsilon}^{n+1/2}(\mathbf{x}_{ij}) = \tilde{f}_{\alpha, \varepsilon}^{+,n}(\mathbf{x}'_{ij}). \quad (20)$$

To evaluate the interface flux  $\mathbf{F}_{\alpha, \varepsilon, i}^{n+1/2}$ , we assume that the electron distribution function varies linearly in each cell to reconstruct the auxiliary function  $\tilde{f}_{\alpha, \varepsilon}^{+,n}(\mathbf{x}'_{ij})$  in Eq. (20), as shown in Fig. 1; then

$$\tilde{f}_{\alpha, \varepsilon}^{+,n}(\mathbf{x}'_{ij}) = \tilde{f}_{\alpha, \varepsilon}^{+,n}(\mathbf{x}_c) + (\mathbf{x}'_{ij} - \mathbf{x}_c) \cdot \boldsymbol{\sigma}_c, \quad (21)$$

where  $\boldsymbol{\sigma}_c$  is the slope of the auxiliary function  $\tilde{f}_{\alpha, \varepsilon}^{+,n}(\mathbf{x}'_{ij})$  in the cell where  $\mathbf{x}_c$  is located. We have  $c = i$  if  $\mathbf{v}_{\alpha} \cdot \mathbf{n}_{ij} > 0$  and  $c = j$  otherwise. For smooth problems,  $\boldsymbol{\sigma}_c$  can be obtained using central difference, and for discontinuities, it can be constructed using methods such as the van Leer limiter to ensure

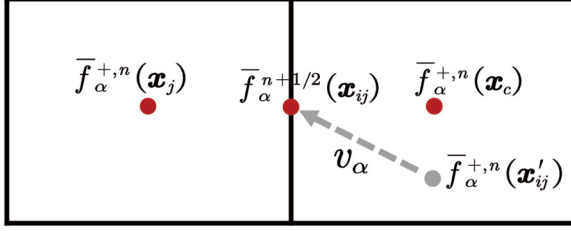


FIG. 1. Schematic of the reconstructed distribution function at the interface.

numerical accuracy and stability. In the one-dimensional (1D) case, the van Leer limiter is defined as

$$\sigma_i = [\text{sgn}(s_1) + \text{sgn}(s_2)] \frac{|s_1||s_2|}{|s_1| + |s_2|}, \quad (22)$$

where

$$s_1 = \frac{\bar{f}_{\alpha,\varepsilon,i}^{+,n} - \bar{f}_{\alpha,\varepsilon,i-1}^{+,n}}{x_i - x_{i-1}}, \quad s_2 = \frac{\bar{f}_{\alpha,\varepsilon,i+1}^{+,n} - \bar{f}_{\alpha,\varepsilon,i}^{+,n}}{x_{i+1} - x_i}. \quad (23)$$

As a result, the original distribution function  $f_{\alpha,\varepsilon}^{n+1/2}(\mathbf{x}_{ij})$  can be obtained from Eqs. (18), (20), and (21):

$$f_{\alpha,\varepsilon}^{n+1/2}(\mathbf{x}_{ij}) = \frac{4\tau}{4\tau + \Delta t} \bar{f}_{\alpha,\varepsilon}^{n+1/2}(\mathbf{x}_{ij}) + \frac{\Delta t}{4\tau + \Delta t} f_{0,\alpha,\varepsilon}^{n+1/2}(\mathbf{x}_{ij}), \quad (24)$$

where  $f_{0,\alpha,\varepsilon}^{n+1/2}(\mathbf{x}_{ij})$  is a function of  $\mu_{\text{loc},ij}^{n+1/2}$  and  $T_{\text{loc},ij}^{n+1/2}$ , which can be obtained with the particle number and energy conservation of the scattering operator. Since the original distribution function  $f$  in Eqs. (6) and (7) is unknown, the conservation equation needs to be converted to the form of  $\bar{f}$  from Eqs. (6), (7), and (18):

$$\int_{\Omega_d} \int_{-\infty}^{+\infty} \psi^U \frac{D(\varepsilon)}{\Omega_d} \left[ \frac{(4\tau^N + \Delta t) f_{0,ij}^{U,n+1/2} - \Delta t f_{0,ij}^{N,n+1/2}}{(4\tau + \Delta t)(\tau^U + \tau^N)} - \frac{4\tau \bar{f}_{ij}^{n+1/2}}{(4\tau + \Delta t)\tau^U} \right] d\varepsilon d\Omega = \mathbf{0}, \quad (25)$$

$$\int_{\Omega_d} \int_{-\infty}^{+\infty} \psi^N \frac{D(\varepsilon)}{\Omega_d} \left[ \frac{(4\tau^N + \Delta t) f_{0,ij}^{N,n+1/2} - \Delta t f_{0,ij}^{U,n+1/2}}{(4\tau + \Delta t)(\tau^U + \tau^N)} - \frac{4\tau \bar{f}_{ij}^{n+1/2}}{(4\tau + \Delta t)\tau^N} \right] d\varepsilon d\Omega = \mathbf{0}. \quad (26)$$

If multiple bands contribute to the transport, the above equation should also include a summation over band indices. In this way, the interface flux  $\mathbf{F}_{\alpha,\varepsilon,i}^{n+1/2}$  is fully determined by Eqs. (13) and (24). From Eq. (16) we can obtain the distribution function  $\bar{f}_{\alpha,\varepsilon,i}^{n+1}$  at  $t_{n+1}$ . Similarly,  $T_{\text{loc},i}^{n+1}$  and  $\mu_{\text{loc},i}^{n+1}$  can be determined from the following two equations:

$$\int_{\Omega_d} \int_{-\infty}^{+\infty} \psi^U \frac{D(\varepsilon)}{\Omega_d} \left[ \frac{(2\tau^N + \Delta t) f_{0,i}^{U,n+1} - \Delta t f_{0,i}^{N,n+1}}{(2\tau + \Delta t)(\tau^U + \tau^N)} - \frac{2\tau \bar{f}_i^{n+1}}{(2\tau + \Delta t)\tau^U} \right] d\varepsilon d\Omega = \mathbf{0}, \quad (27)$$

$$\int_{\Omega_d} \int_{-\infty}^{+\infty} \psi^N \frac{D(\varepsilon)}{\Omega_d} \left[ \frac{(2\tau^N + \Delta t) f_{0,i}^{N,n+1} - \Delta t f_{0,i}^{U,n+1}}{(2\tau + \Delta t)(\tau^U + \tau^N)} - \frac{2\tau \bar{f}_i^{n+1}}{(2\tau + \Delta t)\tau^N} \right] d\varepsilon d\Omega = \mathbf{0}. \quad (28)$$

To solve Eqs. (25)–(28), we use the Newtonian iteration method. The electric and heat currents in the center of each cell can be expressed as

$$\mathbf{J}(\mathbf{x}_i, t) = -e \int_{\Omega_d} \int_{\varepsilon_{\min}}^{\varepsilon_{\max}} \mathbf{v} \frac{D(\varepsilon)}{\Omega_d} \frac{2\tau(\varepsilon)}{2\tau(\varepsilon) + \Delta t} \bar{f}(\mathbf{x}_i, t) d\varepsilon d\Omega, \quad (29)$$

$$\mathbf{J}_q(\mathbf{x}_i, t) = \int_{\Omega_d} \int_{\varepsilon_{\min}}^{\varepsilon_{\max}} [\varepsilon - \bar{\mu}(\mathbf{x}_i, t)] \times \mathbf{v} \frac{D(\varepsilon)}{\Omega_d} \frac{2\tau(\varepsilon)}{2\tau(\varepsilon) + \Delta t} \bar{f}(\mathbf{x}_i, t) d\varepsilon d\Omega. \quad (30)$$

It is notable that the distribution functions  $\bar{f}^+$ ,  $\bar{f}^-$ , and  $\bar{f}$  satisfy the following relationship, which simplifies the calculation:

$$\bar{f}^+ = \frac{4}{3} \bar{f}^- - \frac{1}{3} \bar{f}. \quad (31)$$

Importantly, in the DUGKS, the time step  $\Delta t$  is determined by the Courant-Friedrichs-Lewy (CFL) condition

$$\Delta t = \gamma \min \left( \frac{\Delta x}{\mathbf{v}} \right), \quad (32)$$

where  $\gamma \in (0, 1)$  is the CFL number, such that the defined time step remains consistent for any relaxation time and has the AP property.

The procedure of the present DUGKS can be summarized as follows:

- (1) Set the initial temperature  $T_0$ , chemical potential  $\mu_0$ , discrete energy space, real space, and solid angle space, and set the initial distribution function  $\bar{f}_{\alpha,\varepsilon,i}^n$  according to Eq. (14).
- (2) Calculate  $\bar{f}_{\alpha,\varepsilon,i}^{+,n}$  and its slope  $\sigma_c$ , and construct the distribution function  $\bar{f}_{\alpha,\varepsilon}^{+,n}(\mathbf{x}'_{ij})$  according to Eq. (21).
- (3) Calculate the interface distribution  $\bar{f}_{\alpha,\varepsilon}^{n+1/2}(\mathbf{x}_{ij})$  based on Eq. (22).
- (4) Calculate the local temperature  $T_{\text{loc},ij}^{n+1/2}$  and local chemical potential  $\mu_{\text{loc},ij}^{n+1/2}$  at the cell interface based on Eqs. (25) and (26) to obtain the corresponding equilibrium distribution  $f_{0,\alpha,\varepsilon}^{n+1/2}(\mathbf{x}_{ij})$ .
- (5) Calculate the original distribution function  $f_{0,\alpha,\varepsilon}^{n+1/2}(\mathbf{x}_{ij})$  at the cell interface based on Eq. (24), and update the cell interface flux  $\mathbf{F}_{\alpha,\varepsilon,i}^{n+1/2}$  by Eq. (13).
- (6) Calculate  $\bar{f}_{\alpha,\varepsilon,i}^{+,n}$  based on Eq. (31) to update  $\bar{f}_{\alpha,\varepsilon,i}^{n+1}$  at the new time step using Eq. (16).
- (7) Update the temperature  $T_{\text{loc},i}^{n+1}$  and chemical potential  $\mu_{\text{loc},i}^{n+1}$  of the cell at the next time step based on Eqs. (27) and (28).
- (8) Repeat steps 2 to 7 until the stop criterion is reached.

### Boundary conditions

For isothermal boundary conditions, electrons colliding with the boundary are absorbed, while an electron in equilibrium at the boundary temperature  $T_b$  and chemical potential  $\mu_b$  is emitted into the computational domain,

$$f(\mathbf{x}_b, \varepsilon, \mathbf{s}) = f_0(T_b, \mu_b, \varepsilon), \quad \mathbf{s} \cdot \mathbf{n}_b > 0, \quad (33)$$

where  $\mathbf{n}_b > 0$  is the unit normal vector pointing from the interface to the domain.

For periodic boundary conditions, driven by the temperature and/or chemical potential gradient, an electron leaves one boundary while another electron with the same velocity and energy enters the domain from the corresponding periodic boundary. The distribution of these two electrons deviates equally from the equilibrium state at the passing boundary,

$$\begin{aligned} f(\mathbf{x}_{b1}, \varepsilon, \mathbf{s}) - f_0(T_{b1}, \mu_{b1}, \varepsilon) \\ = f(\mathbf{x}_{b2}, \varepsilon, \mathbf{s}) - f_0(T_{b2}, \mu_{b2}, \varepsilon), \end{aligned} \quad (34)$$

where  $b1$  and  $b2$  denote the corresponding periodic boundaries.

For the diffusive reflection boundary, it is assumed that electrons reflected from the boundary are isotropic:

$$f(\mathbf{x}_b, \varepsilon, \mathbf{s}) = \frac{\int_{\mathbf{s}' \cdot \mathbf{n}_b < 0} (\mathbf{s}' \cdot \mathbf{n}_b) f(\mathbf{x}_b, \varepsilon, \mathbf{s}') d\Omega}{\int_{\mathbf{s}' \cdot \mathbf{n}_b > 0} \mathbf{s}' \cdot \mathbf{n}_b d\Omega}, \quad \mathbf{s} \cdot \mathbf{n}_b > 0. \quad (35)$$

Meanwhile, for the specular reflection boundary, we have

$$f(\mathbf{x}_b, \varepsilon, \mathbf{s}) = f(\mathbf{x}_b, \varepsilon, \mathbf{s}''), \quad \mathbf{s} \cdot \mathbf{n}_b > 0, \quad (36)$$

where  $\mathbf{s}'' = \mathbf{s} - 2(\mathbf{s} \cdot \mathbf{n}_b)\mathbf{n}_b$ . It is noted that for both diffusive and specular boundaries no energy and particle exchanges occur at the interface, and they are therefore also called adiabatic boundaries.

## IV. NUMERICAL RESULTS

In this section, numerical calculations of four types of problems are performed to test the performance of the DUGKS. For the first two examples, we consider the cross-plane (Sec. IV A) and in-plane (Sec. IV B) electron transport of the Au films to verify the DUGKS solution against the deviational MC scheme available in the literature [26]. In the third example (Sec. IV C), we consider hydrodynamic transport in 2D systems using the parameters of graphene. In the last example (Sec. IV D), we consider quasi-1D thermoelectric transport in model metal and semiconductor systems.

For the generality of the program, we use the van Leer limiter to construct the gradient  $\sigma_c$ . In all calculations, we take into account electrons in the energy window of  $[\mu_+ + 15k_B T_0, \mu_- - 15k_B T_0]$ , with  $\mu_+$  and  $\mu_-$  being the higher and lower chemical potentials, respectively. The energy window is uniformly discretized. The grid number is denoted as  $N_\varepsilon$ . In the solid angle space,  $\theta$  and  $\varphi$  are discretized into the  $N_\theta$  and  $N_\varphi$  subdirections using the GL rule. The weights and coordinates of the GL quadrature can be computed using a standard computer code [41].

Note that if real physical quantities are used in the computation, large round-off errors may occur due to the large

disparity of their magnitudes. Therefore, dimensionless quantities are employed in our computation, where the following nondimensional variables are employed:

$$\begin{aligned} \varepsilon^* &= \frac{\varepsilon}{\varepsilon_F}, \quad \mu^* = \frac{\mu}{\varepsilon_F}, \quad T^* = \frac{T}{T_0}, \quad \mathbf{p}^* = \frac{\mathbf{p}}{\hbar k_F}, \\ \mathbf{u}^* &= \frac{\hbar k_F}{\varepsilon_F} \mathbf{u}, \quad \mathbf{r}^* = \frac{\mathbf{r}}{L_{\text{ref}}}, \quad t^* = \frac{v_F t}{L_{\text{ref}}}, \quad \mathbf{v}^* = \frac{\mathbf{v}}{v_F}, \\ \text{Kn}^U &= \frac{v_F \tau^U}{L_{\text{ref}}}, \quad \text{Kn}^N = \frac{v_F \tau^N}{L_{\text{ref}}}, \end{aligned}$$

where  $*$  denotes that the quantity is dimensionless (omitted in the text for ease of presentation);  $\text{Kn}^U$  and  $\text{Kn}^N$  are the Knudsen numbers of the umklapp process and the normal process;  $\varepsilon_F$ ,  $k_F$ , and  $v_F$  are the Fermi energy, Fermi wave vector, and Fermi velocity, respectively; and  $L_{\text{ref}}$  is the characteristic length.

### A. Cross-plane electron thermal transport

The reciprocal lattice of Au is of the bcc type, and the first Brillouin zone is a truncated octahedron. The Fermi surface, although distorted along the  $\langle 111 \rangle$  direction, is approximately spherical, so we use the nearly free electron model  $\varepsilon = \hbar^2 \mathbf{k}^2 / (2m)$  and set the Fermi energy to  $\varepsilon_F = 5.51$  eV. To make a comparison with the analytical results, we focus on only the umklapp processes and set  $\tau^U = 27.7 \sqrt{\varepsilon} / \varepsilon_F$  fs and  $\tau^N \rightarrow \infty$ . The CFL number is fixed at 0.7. The average temperature  $T_0$  is set to 300 K.

We first consider the cross-plane ( $x$  direction) electron thermal transport. The structure is shown in Fig. 2(a). This is a quasi-1D problem since the system is translationally invariant in the  $y$  and  $z$  directions. We use isothermal boundary conditions with  $T_L = T_0 + \Delta T_L$  and  $T_R = T_0 + \Delta T_R$ . When  $\Delta T_L$  and  $\Delta T_R$  are relatively small, the distribution function can be linearized as  $f \approx C_T \Delta T + C_\mu \Delta \mu$ , with  $C_T = \partial f_0 / \partial T$  and  $C_\mu = \partial f_0 / \partial \mu$ . A semianalytical solution can then be obtained using the linear approximation, following Ref. [42],

$$\begin{aligned} 2 \int_{\varepsilon_{\min}}^{\varepsilon_{\max}} \frac{D(\varepsilon)}{\tau(\varepsilon)} \begin{pmatrix} \varepsilon C_T & \varepsilon C_\mu \\ C_T & C_\mu \end{pmatrix} d\varepsilon \begin{pmatrix} \Delta T(\hat{x}) \\ \Delta \mu(\hat{x}) \end{pmatrix} \\ = F(\hat{x}) + \int_0^1 K(\hat{x}, \hat{x}') \begin{pmatrix} \Delta T(\hat{x}) \\ \Delta \mu(\hat{x}) \end{pmatrix} d\hat{x}'. \end{aligned} \quad (37)$$

This is the second type of Fredholm integral equation, with  $\hat{x} = x/L$  being the dimensionless coordinate and

$$\begin{aligned} F(\hat{x}) &= \int_{\varepsilon_{\min}}^{\varepsilon_{\max}} \frac{D(\varepsilon)}{\tau(\varepsilon)} \begin{pmatrix} \varepsilon C_T & \varepsilon C_\mu \\ C_T & C_\mu \end{pmatrix} \left[ E_2 \left( \frac{\hat{x}}{\text{Kn}_\varepsilon} \right) \begin{pmatrix} \Delta T_L \\ \Delta \mu_L \end{pmatrix} \right. \\ &\quad \left. + E_2 \left( \frac{1 - \hat{x}}{\text{Kn}_\varepsilon} \right) \begin{pmatrix} \Delta T_R \\ \Delta \mu_R \end{pmatrix} \right] d\varepsilon, \\ K(\hat{x}, \hat{x}') &= \int_{\varepsilon_{\min}}^{\varepsilon_{\max}} \frac{D(\varepsilon)}{\text{Kn}_\varepsilon \tau(\varepsilon)} E_1 \left( \frac{|\hat{x} - \hat{x}'|}{\text{Kn}_\varepsilon} \right) \begin{pmatrix} \varepsilon C_T & \varepsilon C_\mu \\ C_T & C_\mu \end{pmatrix} d\varepsilon. \end{aligned} \quad (38)$$

Here,  $E_n(x) = \int_0^1 \theta^{n-2} \exp(-x/\theta) d\theta$ , and  $\text{Kn}_\varepsilon = v_\varepsilon \tau_\varepsilon / L$  is the energy-dependent Knudsen number. From the above equations, we can obtain  $\Delta T(\hat{x})$  and  $\Delta \mu(\hat{x})$  using the degenerate kernel method.

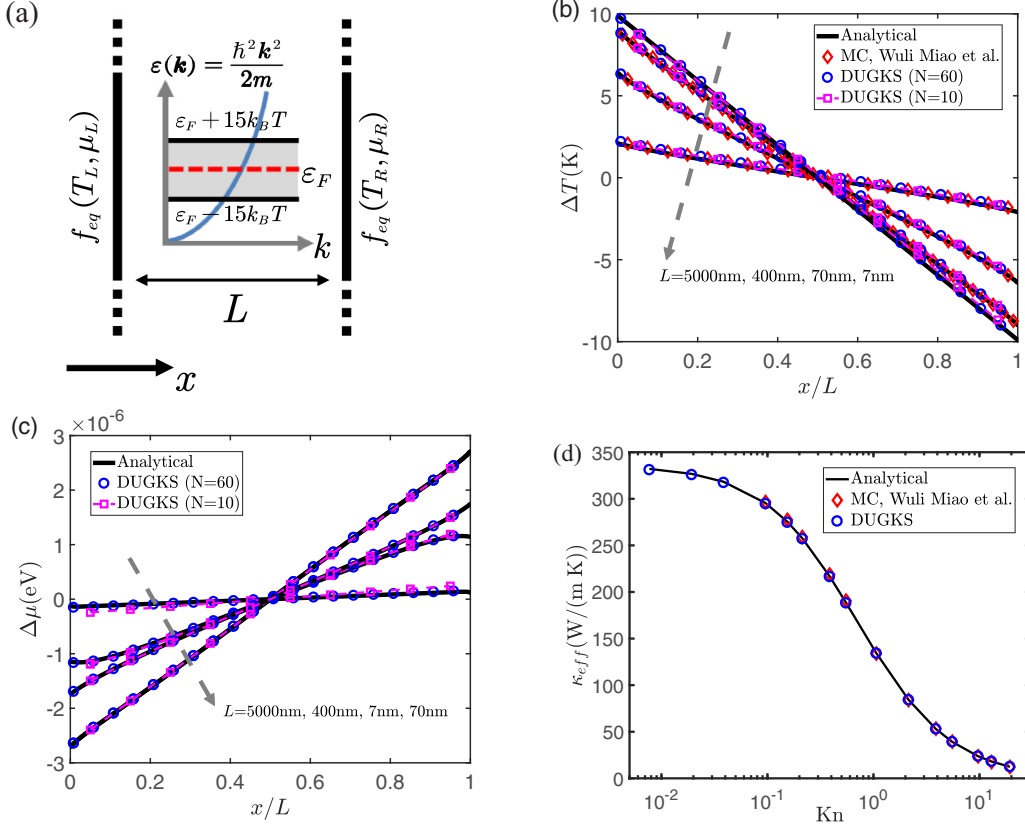


FIG. 2. Cross-plane electron thermal transport in Au films. (a) Schematic of the system setup. The energy band structure is shown in the middle. The gray area is the energy range considered in the calculation. We choose  $\Delta T_L = -\Delta T_R = 10$  K without initial chemical potential difference. (b) Steady-state temperature distribution, (c) steady-state chemical potential distribution, and (d) variation of the effective thermal conductivity with the Knudsen number.

We can then calculate the steady-state heat flux density as

$$J_q = \int \int_0^1 (\varepsilon - \varepsilon_F) f^+ v \theta d\theta d\varepsilon - \int \int_0^1 (\varepsilon - \varepsilon_F) f^- v \theta d\theta d\varepsilon, \quad (40)$$

where  $f^+$  and  $f^-$  describe the forward and backward transport of electrons, respectively, and can be written as

$$f^+(\hat{x}) = (C_T \Delta T_L + C_\mu \Delta \mu_L) e^{-\frac{\hat{x}}{\text{Kn}_e \theta}} + \int_0^{\hat{x}} \frac{C_T \Delta T(\hat{x}') + C_\mu \Delta \mu(\hat{x}')}{\text{Kn}_e \theta} e^{\frac{\hat{x}' - \hat{x}}{\text{Kn}_e \theta}} d\hat{x}', \quad (41)$$

$$f^-(\hat{x}) = (C_T \Delta T_R + C_\mu \Delta \mu_R) e^{-\frac{1 - \hat{x}}{\text{Kn}_e \theta}} + \int_{\hat{x}}^1 \frac{C_T \Delta T(\hat{x}') + C_\mu \Delta \mu(\hat{x}')}{\text{Kn}_e \theta} e^{\frac{\hat{x}' - \hat{x}}{\text{Kn}_e \theta}} d\hat{x}'. \quad (42)$$

The effective thermal conductivity of the system is then obtained from

$$\kappa_{\text{eff}} = L J_q / |T_L - T_R|. \quad (43)$$

Different transport regimes can be characterized by the Knudsen number  $\text{Kn} = \lambda / L_{\text{ref}}$ , where  $\lambda$  is the electron mean free path. When  $\text{Kn} \ll 1$ , electrons are frequently scattered and exhibit diffusive transport; when  $\text{Kn} \gg 1$ , they move through the material almost without scattering and exhibit

ballistic transport. We consider several different lengths,  $L = 5 \mu\text{m}$ , 400 nm, 70 nm, and 7 nm. The corresponding  $\text{Kn}$  are 0.0077, 0.096, 0.55, and 5.5, respectively, going from the diffusive to ballistic regime. We compare our numerical results with the above semianalytical solution and deviational MC results [26]. The solid angle is discretized into  $N_\theta = 100$  subdirections using the GL rule, and the system in the  $x$  direction is uniformly discretized to  $N = 60$  and 10, respectively. The results are shown in Figs. 2(b)–(d). Figure 2(b) shows that as the film size decreases, the system deviates from Fourier's law, and the boundary temperature slip becomes significant. As the mean free path of electrons increases, the electrons moving to the boundary are not sufficiently thermalized and strongly scatter with the electrons emitted from the boundary, giving rise to a nonlinear temperature distribution. Our scheme also captures the temperature-induced change in the chemical potential [Fig. 2(c)], caused by the thermoelectric effect. For a small temperature difference, this change is so tiny that we can ignore it when considering electron thermal transport. However, this small change is an essential factor in maintaining particle number conservation. The behavior of the effective thermal conductivity [Fig. 2(d)] is similar to that in the phonon case, with enhanced boundary scattering suppressing the thermal conductivity as the film thickness decreases.

Thus, we find good agreement of our numerical results with the analytical solutions in the whole range from ballistic

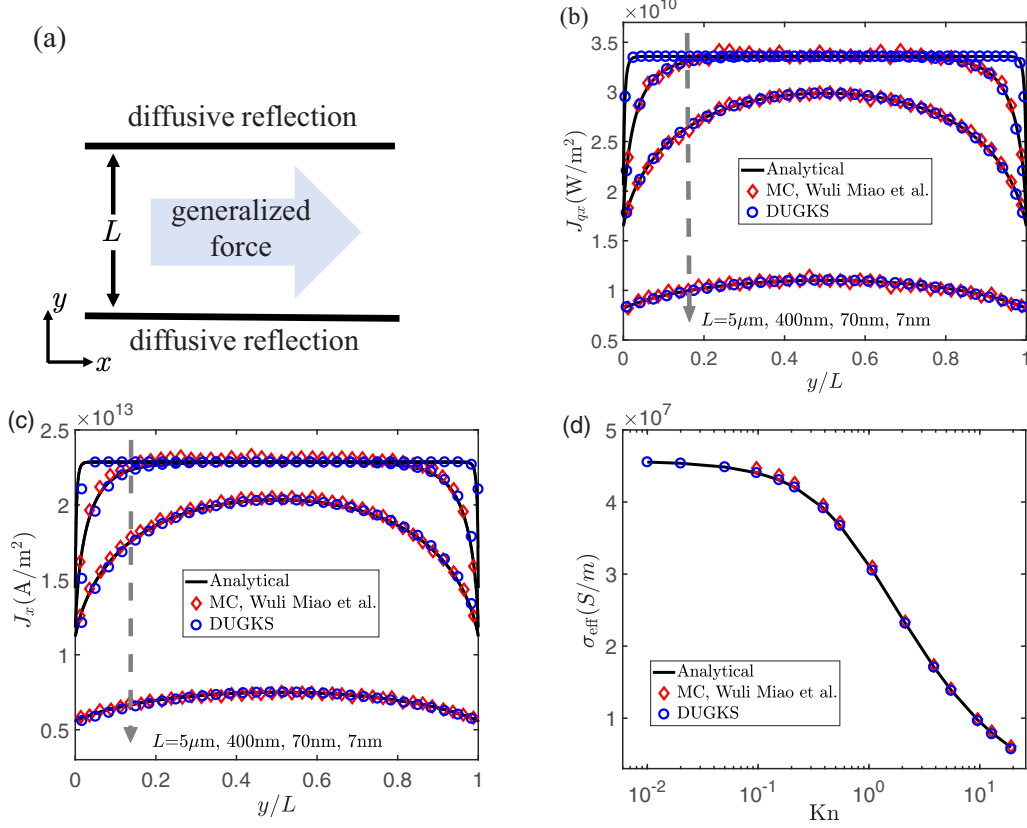


FIG. 3. In-plane electrical and thermal transport in Au films, with  $L = 5 \mu\text{m}$ ,  $400 \text{ nm}$ ,  $70 \text{ nm}$ , and  $7 \text{ nm}$ , covering both diffusive and ballistic transport regimes. The real space grids are set to  $N_x \times N_y = 2 \times 60$ , and the solid angle grids are  $N_\theta \times N_\phi = 40 \times 40$ . (a) Schematic of the transport setup. (b) Heat flux density  $J_{qx}$  distribution along  $y$  driven by the temperature gradient in the  $x$  direction. (c) Current density  $J_x$  distribution along  $y$  driven by a chemical potential gradient in the  $x$  direction. (d) The effective conductivity  $\sigma_{\text{eff}} = e\bar{J}_x/(d\mu/dx)$  as a function of the Knudsen number. Here,  $\bar{J}_x$  is the average of  $J_x$  along  $y$ .

to diffusive transport, with good convergence on multiscale numerical simulations. Due to the coupled treatment of drift and scattering, in our scheme the mesh size does not have to be smaller than the particle mean free path. The results converge well even for sparse meshes with  $N = 10$ . In addition, the time step  $\Delta t$  is completely determined by the CFL number and is not constrained by the relaxation time. These results illustrate that the scheme has the AP property. Also, the efficiency comparison with the DOM confirms the multiscale nature of the DUGKS (see Appendix B).

### B. In-plane electron transport

In this section, as an example of quasi-2D transport, we calculate the in-plane thermal and electrical transport properties in Au thin films. The system setup is shown in Fig. 3(a). We use the diffusive boundaries for the top and bottom and periodic boundaries for the left and right sides. Due to the applied generalized forces (e.g., temperature or chemical potential gradient), the distribution function deviates from the equilibrium one and is written as  $f = f_0 + f_1$ , with  $f_0$  being the equilibrium part and  $f_1$  being a small deviation. It can be described by the Fuchs-Sondheimer theory [43,44]:

$$f_1 = \begin{cases} -v_y \tau \left( \frac{\partial f_0}{\partial T} \frac{dT}{dy} + \frac{\partial f_0}{\partial \mu} \frac{d\mu}{dy} \right) \left[ 1 - \exp\left(-\frac{x}{\tau v_x^>} \right) \right], \\ -v_y \tau \left( \frac{\partial f_0}{\partial T} \frac{dT}{dy} + \frac{\partial f_0}{\partial \mu} \frac{d\mu}{dy} \right) \left[ 1 - \exp\left(-\frac{L-x}{\tau v_x^<} \right) \right], \end{cases} \quad (44)$$

where  $v_x^>$  and  $v_x^<$  denote the cases of  $v_x > 0$  and  $v_x < 0$ , respectively. The electrical and heat flux densities can be calculated from  $f_1$ .

We consider the temperature- and chemical-potential-driven cases separately. The results for the temperature-driven case with  $dT/dx = -0.1 \text{ K/nm}$  are shown in Fig. 3(b). This scheme again accurately captures the heat transfer process at different Knudsen numbers. In contrast to MC, the DUGKS results are free from random errors, and the mean free path does not limit the mesh size. The heat flux density saturates at  $L = 5 \mu\text{m}$ , corresponding to diffusive transport, following Fourier's law. The suppression of heat flux at the boundaries is due to inelastic scattering occurring at the diffusive reflection boundary. The heat flux density distribution becomes uniform again in the ballistic regime. For the chemical-potential-driven case, with  $d\mu/dx = -e\nabla\phi$  and  $-\nabla\phi = 5 \times 10^5 \text{ V/m}$ , the results are shown in Figs. 3(c)–(d). The agreement with analytical solutions again demonstrates the accuracy of this multiscale scheme.

### C. dc and ac hydrodynamic transport

In this section, we calculate dc and ac electronic transport in a 2D sheet using the parameters for graphene. Assuming heavy  $n$  type doping, we consider only the contribution from the upper band with the linear dispersion relation

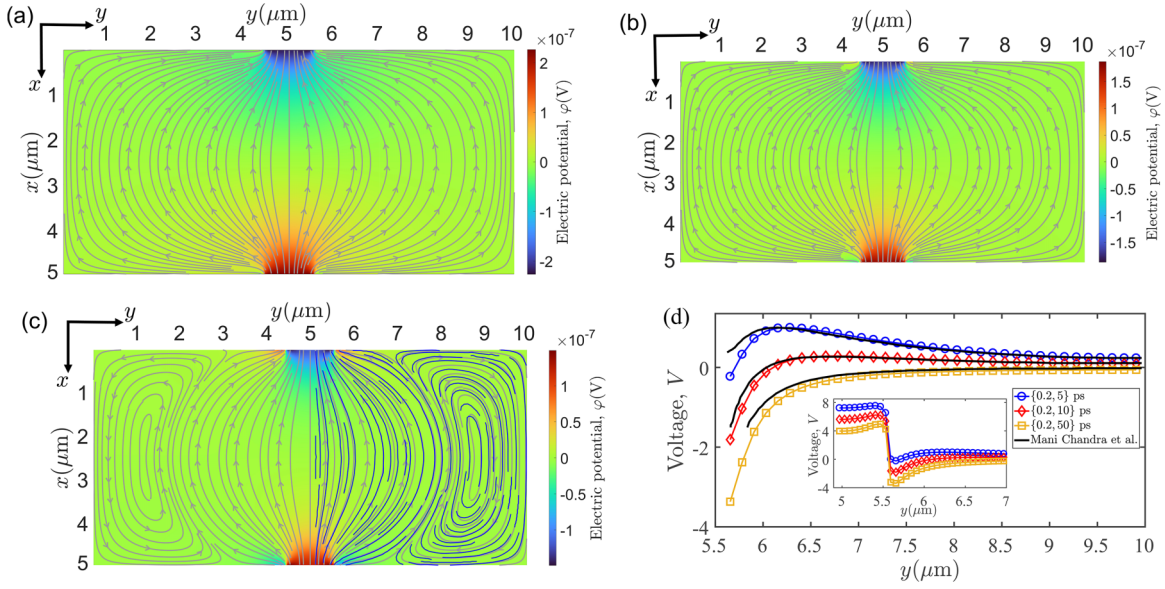


FIG. 4. dc and ac hydrodynamic transport in a 2D sheet of size  $5 \times 10 \mu\text{m}^2$ . We use  $N_\varepsilon = 80$  and  $N_x \times N_y = 80 \times 160$  for energy and real space, respectively. For 2D angle space, we use  $N_\varphi = 400$ . Potential distribution and current lines for  $\{\tau^N, \tau^U\} =$  (a)  $\{0.2, 5\}$  ps, (b)  $\{0.2, 10\}$  ps, and (c)  $\{0.2, 50\}$  ps; the darker line in (c) is the result from Chandra *et al.* [17]. (d) The potential difference between the lower and upper boundaries at  $y \in [5.7, 10] \mu\text{m}$ . We scaled the results for other cases by setting the maximum value from the parameter set  $\{0.2, 5\}$  ps to 1. The inset shows the potential distribution at  $y \in [5.5, 7] \mu\text{m}$ , where the jump in value can be observed.

$\varepsilon(k) = \hbar v_F k$ , where  $v_F \approx 10^6$  m/s is the Fermi velocity. Since hydrodynamic transport takes place at relatively low temperatures, we set  $T_0 = 10$  K and  $\mu_0 = 10.8$  meV. We assume that dc driving and ac driving locate in the center of the left and right boundaries, with a width of  $1 \mu\text{m}$ . We adopt the same boundary conditions as Ref. [17]. Specifically, for dc calculations, we set an isothermal boundary for the drift velocity  $u_{x0}^L = u_{x0}^R = 10^{-4} v_F$  distributed at the injections, and for ac calculations, we set an isothermal boundary for  $u_{x0}^L = u_{x0}^R = 10^{-4} v_F \sin(2\pi f t)$ , where  $f = 10$  GHz is the frequency of the ac driving. For the other boundaries, we use specular reflection. For such problems, one is often interested in the voltage or potential of the system. In our framework, we can obtain the potential with  $\varphi(\mathbf{r}, t) = -\mu(\mathbf{r}, t)/e + \mu_0/e$ . We calculated the hydrodynamic transport dominated by the normal processes for the three cases with  $\{\tau^N, \tau^U\} = \{0.2, 5\}$  ps,  $\{0.2, 10\}$  ps, and  $\{0.2, 50\}$  ps. The results are shown in Figs. 4(a)–4(c). Although all three sets of relaxation times are dominated by normal processes, only results from the third parameter set show vortices. The positions of the vortices are consistent with the results of Mani *et al.* [17], and nonlocal negative resistance is also observed [Fig. 4(d)].

For ac transport, we considered two sets of parameters,  $\{0.2, 1\}$  ps and  $\{0.2, 5\}$  ps. The DUGKS again accurately captures the voltage transients [Fig. 5(a)]. Figure 5(b) shows that, for the Ohmic transport, the phase  $\phi(y) = \phi[I_d, \varphi(y)]$  follows the source current at any position, but for the hydrodynamic transport it consistently delayed from the source current.

#### D. Thermoelectric transport

In this section, we consider thermoelectric transport in model metals and semiconductors with  $L = 200$  nm. The left and right chemical potentials are set to  $\mu_L = \varepsilon_F + \Delta\mu/2$

and  $\mu_R = \varepsilon_F - \Delta\mu/2$ , where  $\Delta\mu$  is 10, 20, and 40 meV. For semiconductors, we use the effective mass approximation  $\varepsilon = \hbar^2 k^2 / 2m^*$ , with  $m^*$  being the electron effective mass. We assume that the semiconductor is isotropic and  $n$  doped with a conduction band effective mass  $m^* = 0.068m$ . The Fermi energy level is located  $\Delta = 0.05$  eV below the conduction band bottom. For both metals and semiconductors, the energy, real, and angle space grids are set to  $N_\varepsilon = 80$ ,  $N = 80$ ,  $N_\theta = 100$ , respectively. We considered both umklapp ( $\tau^U = 0.01$  ps,  $\tau^N = 1$  s) and normal ( $\tau^U = 1$  s,  $\tau^N = 0.01$  ps) dominated cases.

Although there is no analytical solution, we can interpret the results qualitatively using a first-order approximation of the eBTE. With the umklapp processes dominating, it is described as

$$\begin{pmatrix} \mathbf{J} \\ \mathbf{J}_q \end{pmatrix} = \begin{pmatrix} eK_0 & -eK_1/T \\ -K_1 & K_2/T \end{pmatrix} \begin{pmatrix} \nabla\mu \\ -\nabla T \end{pmatrix} \quad (45)$$

and

$$K_n = \frac{\tau}{3} \iint v v D(\varepsilon) (\varepsilon - \mu)^n \left( -\frac{\partial f_0}{\partial \varepsilon} \right) d\varepsilon d\Omega. \quad (46)$$

In fact, Eq. (45) neglects the impact of boundary conditions, making it valid only in regions far from the boundaries [45]. Thus, we describe the region of  $x \in [5, 195]$  nm by Eq. (45).

The results for the metal in the umklapp-process-dominated case are shown in Figs. 6(a) and 6(b). The temperature distribution takes the form of a quadratic function, with the peak occurring at  $L/2$ . This is expected when Joule heating is dominant [46]. In this case, using Eq. (45), we can obtain a formal solution for  $T(x)$ :

$$T(x) = -\frac{\bar{T}}{K_2} \frac{d\mu}{dx} \left( \frac{J}{e} x^2 - \frac{J}{e} x_0 x + K_1 x \right) + T_0 + \Delta T_C, \quad (47)$$

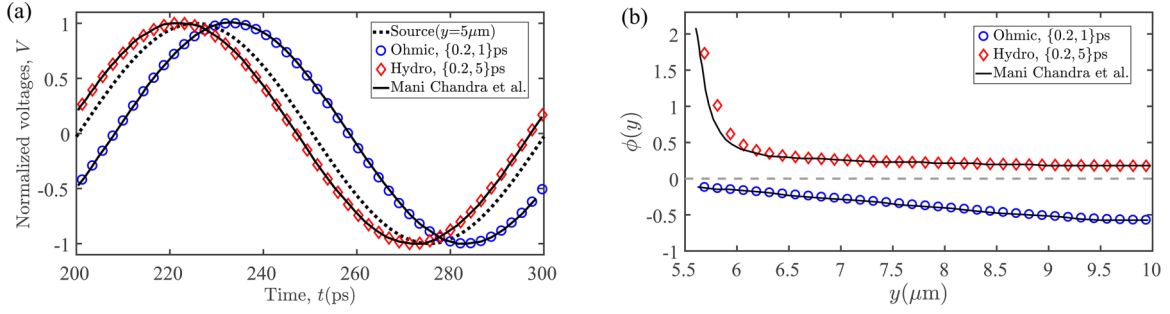


FIG. 5. (a) Change in normalized potential at  $y = 9 \mu\text{m}$  from  $t = 200$  ps to  $t = 300$  ps. (b) Phase difference of the potential wave form at  $y \in [5.7, 10] \mu\text{m}$  with respect to  $y = 5 \mu\text{m}$  (i.e., the source current).

where  $\Delta T_C$  is the temperature jump due to the thermal resistance of the interface and  $x_0$  is the zero point of the heat flux. We neglect the spatial dependence of  $K_n$  in obtaining Eq. (47) and assume that the chemical potential is linearly distributed. For metals, this applies away from the boundary. The results are shown in Fig. 6(a), which agree well with the numerical results for low chemical potential differences. When  $\Delta\mu = 40$  meV, the large magnitude of the temperature change invalidates the above simple approximation. Now we consider the heat flux density in Fig. 6(b). We note the small deviation of  $x_0$  at  $L/2 + eK_1/J$  from  $L/2$  due to the thermoelectric correction term  $eK_1/J$ . As the chemical potential difference increases,

the zero point shifts toward the center due to the increase in the current density. For  $\Delta\mu = 40$  meV, the effect of the boundary conditions on the results is enhanced, leading to a deviation of the heat flux density close to the boundary.

The results for the metal when the normal process dominates are shown in Figs. 6(c) and 6(d). The presence of drift velocity  $\mathbf{u}$  further complicates the results. Since the momentum conservation of the normal process does not generate thermal resistance, the temperature distribution should be homogeneous. However, the presence of boundary scattering makes the temperature nonuniform [see Fig. 6(c)]. The electrons carry heat in from the left boundary and do not dissipate

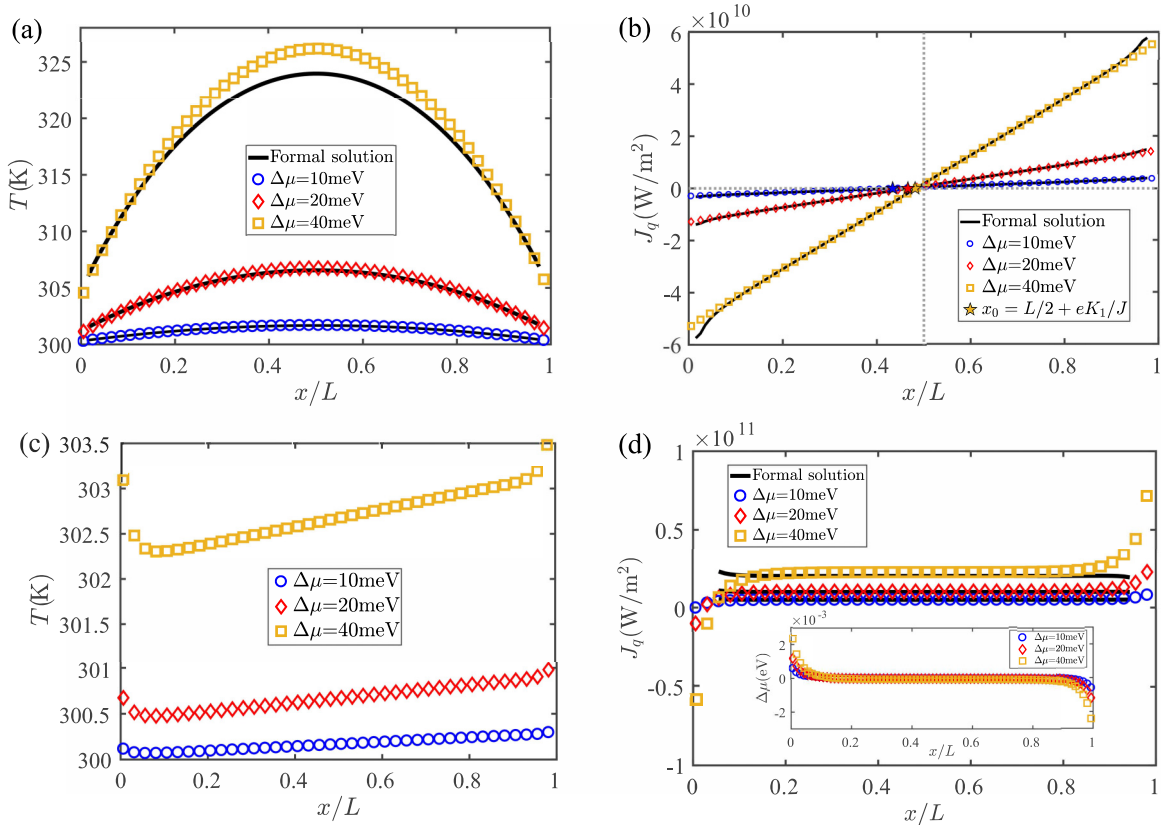


FIG. 6. Numerical results for metal. (a) Temperature distribution due to the chemical potential difference for the umklapp-process-dominated case. (b) The corresponding heat flux density distribution for the situation in (a). (c) Temperature distribution due to the chemical potential difference in the normal-process-dominated case. (d) The corresponding heat flux density distribution for the situation in (c). The inset shows the corresponding chemical potential distribution.

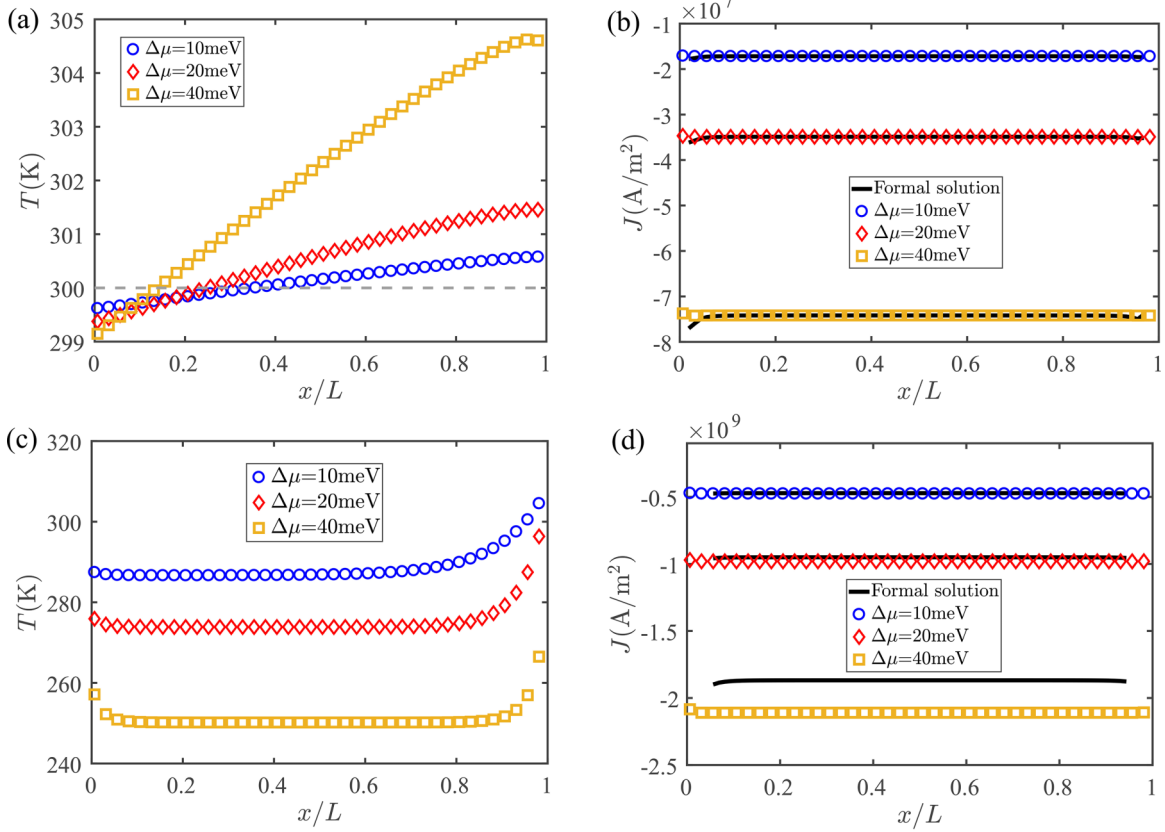


FIG. 7. Numerical results for the semiconductor. (a) Temperature distribution due to the chemical potential difference when the umklapp processes dominate. (b) The corresponding current density distribution for the situation in (a). (c) Temperature distribution in semiconductors due to the chemical potential difference when the normal processes dominate. (d) The corresponding current density distribution for the situation in (c).

heat in the middle. Eventually, the electrons are scattered and release heat at the right boundary, resulting in higher temperatures on the right side than on the left. This nonuniformity becomes evident with the increase of the chemical potential difference. In addition, the temperature increase produced by the normal process is much lower than that of the umklapp process for the same chemical potential difference. The results of the heat flux are shown in Fig. 6(d). They can be understood from the first-order approximation:

$$\begin{aligned} \begin{pmatrix} J \\ J_q \end{pmatrix} &= \frac{1}{3} \iint D(\varepsilon) \begin{pmatrix} -e \\ \varepsilon - \mu \end{pmatrix} \mathbf{v} \cdot \frac{\partial f_0^N}{\partial \mathbf{u}} \Big|_{u=0} d\varepsilon d\Omega \mathbf{u} \\ &+ \begin{pmatrix} eK_0 & -eK_1/T \\ -K_1 & K_2/T \end{pmatrix} \begin{pmatrix} \nabla\mu \\ -\nabla T \end{pmatrix}, \end{aligned} \quad (48)$$

where the first term on the right side is the effect of drift velocity. Since the temperature and chemical potential gradient are small, the contributions to the current and heat flux in the normal process come mainly from  $\mathbf{u}$ . The heat flux generated by the drift velocity term is nearly 2 orders of magnitude higher than the contributions from the temperature and the chemical potential. As in the previous analysis, momentum conservation makes the heat flux gradient zero in the region away from the boundary. The heat flux can also be written as  $\mathbf{J}_q = \mathbf{J}_\varepsilon - \mu\mathbf{J}$ , which satisfies  $\nabla\mathbf{J}_\varepsilon = 0$  and  $\nabla\mathbf{J} = 0$  at the steady state. This implies that the deviation of the heat flux from the first-order approximation arises mainly from the

effect of boundary scattering on the chemical potential [see the inset of Fig. 6(d)].

Results for the semiconductor model are depicted in Fig. 7. The temperature distribution when umklapp processes dominate is shown in Fig. 7(a). Unlike metals, cooling takes place at the left boundary and becomes more apparent as the chemical potential difference increases. This is characteristic of the Peltier effect. The Peltier coefficient is defined as  $\Pi = K_1/(eK_0)$ . From the numerical data, we get an average value of  $\Pi = 0.1$  V. Figure 7(b) shows the corresponding current densities, which are consistent with Eq. (45). For the case in which normal processes dominate [Figs. 7(c) and 7(d)], the conservation of momentum during the collision leads to a uniform decrease of temperature in the region away from the boundary. This cooling phenomenon is more pronounced than the umklapp process [Fig. 7(c)]. The corresponding average Peltier coefficient is  $\Pi = 0.09$  V, similar to the umklapp-dominated case. However, the temperature decreases much more since the current density  $|J|$  is 2 orders of magnitude larger than the case where the umklapp processes dominate [see Figs. 7(b) and 7(d)]. The first-order approximation no longer holds as  $\Delta\mu$  increases to 40 meV.

## V. CONCLUSION

In summary, we developed a discrete unified gas kinetic scheme for the solution of electron Boltzmann transport

TABLE I. Comparison of the computational efficiency of the DUGKS and DOM, where  $t$  is the computational time and  $N_{\text{steps}}$  is the number of computational steps.

$L$ (nm)	DUGKS		DOM	
	$t$ (s)	$N_{\text{steps}}$	$t$ (s)	$N_{\text{steps}}$
10000	101.2	20423	4127.2	128749
5000	53.6	11310	390.1	26619
2000	24.7	5209	41.3	8210
700	10.6	2232	6.9	2184
70	3.1	662	2.3	652
7	6.4	1364	4.7	1360

equation under the Callaway approximation. The coupled treatment of electron drift and scattering makes the cell size and time step independent of the mean free path and relaxation time, which is an advantage in the study of problems with small Knudsen numbers. Numerical results demonstrated that the scheme accurately captures electron transport behaviors across ballistic, hydrodynamic, and diffusive regimes while also exhibiting asymptotic preservation properties. Due to the consideration of the electronic energy band structure and the use of the Newtonian method to solve the energy and particle number conservation equations at the cell interfaces and centers, we were able to simulate different materials across a wide range of parameter regimes. Meanwhile, more complex device shapes and more realistic energy band structures could also be incorporated into our framework in the future. Studying coupled transport including more than one type of quasiparticle, i.e., including a photon-electron-phonon coupled system, is also possible under this generic scheme. However, the dynamics of electrons in  $k$  space needs to be included to study transport under strong electric and magnetic fields. This issue will be discussed in the future.

#### ACKNOWLEDGMENTS

This work was supported by the National Natural Science Foundation of China (Grant No. 22273029) and the Interdisciplinary Research Program of HUST (Grant No. 2023JCYJ002).

#### APPENDIX A: WEAK ELECTRIC FIELD APPROXIMATION

Under an external electric field, the electron follows the following equation of motion:

$$\hbar \dot{\mathbf{k}} = -e(-\nabla\phi), \quad (\text{A1})$$

where  $-e$  is the electron charge and  $\phi$  is the electric potential. Substituting (A1) into Eq. (1), we obtain

$$\frac{\partial f}{\partial t} + \mathbf{v} \cdot \nabla_r f + \mathbf{v} \cdot (e\nabla\phi) \frac{\partial f}{\partial \varepsilon} = \left( \frac{\partial f}{\partial t} \right)_{\text{coll}}. \quad (\text{A2})$$

The spatial dependence of the distribution can be split into that of the chemical potential and that of the temperature,

$$\nabla_r f = \frac{\partial f}{\partial T} \nabla_r T - \frac{\partial f}{\partial \varepsilon} \nabla_r \mu. \quad (\text{A3})$$

TABLE II. The minimal cell size  $\Delta x$  and time step  $\Delta t$  used in Table I, where the mean free path  $\bar{\lambda} = 38.6$  nm and the mean relaxation time  $\bar{\tau} = 0.028$  ps.

$L$ (nm)	DUGKS		DOM	
	$\Delta x$ (nm)	$\Delta t$ (ps)	$\Delta x$ (nm)	$\Delta t$ (ps)
10000	500	$2.1 \times 10^{-1}$	56	$2.3 \times 10^{-2}$
5000	250	$1.0 \times 10^{-1}$	60	$2.5 \times 10^{-2}$
2000	100	$4.2 \times 10^{-2}$	58	$2.5 \times 10^{-2}$
700	35	$1.5 \times 10^{-2}$	35	$1.5 \times 10^{-2}$
70	3.5	$1.5 \times 10^{-3}$	3.5	$1.5 \times 10^{-3}$
7	0.35	$1.5 \times 10^{-4}$	0.35	$1.5 \times 10^{-4}$

The electric field term in Eq. (A2) suggests that it can be absorbed into the spatial dependence of the chemical potential  $\mu$  by defining the electrochemical potential

$$\hat{\mu} = \mu - e\phi. \quad (\text{A4})$$

Then, Eq. (A2) reduces to

$$\frac{\partial f}{\partial t} + \mathbf{v} \cdot \nabla_r f = \left( \frac{\partial f}{\partial t} \right)_{\text{coll}}, \quad (\text{A5})$$

in agreement with Eq. (3) after we apply the Callaway approximation for the collision term.

#### APPENDIX B: COMPARISON OF EFFICIENCY BETWEEN DUGKS AND EXPLICIT DOM

The explicit DOM scheme is currently widely used to solve the Boltzmann transport equation, and it is relatively simple to implement. Here, we compare the computational efficiency between the DUGKS and explicit DOM.

We consider the 1D case to introduce the DOM to solve Eq. (10), where Eq. (10) has the following discrete form:

$$\begin{aligned} & \frac{f_{\alpha,\varepsilon,i}^{n+1} - f_{\alpha,\varepsilon,i}^n}{\Delta t} + v_{\alpha,\varepsilon} \eta \frac{f_{\alpha,\varepsilon,i+1/2}^n - f_{\alpha,\varepsilon,i-1/2}^n}{\Delta x} \\ & = -\frac{f_{\alpha,\varepsilon,i}^n - f_{0,\varepsilon,i}^n}{\tau_\varepsilon}, \end{aligned} \quad (\text{B1})$$

where  $\eta$  is the cosine of the angle between the velocity and the  $x$  axis. In order to improve the spatial accuracy, the cell interface is processed as follows:

$$f_{\alpha,\varepsilon,i+1/2} = \begin{cases} f_{\alpha,\varepsilon,i} + \sigma_i \Delta x / 2 & \eta > 0, \\ f_{\alpha,\varepsilon,i+1} - \sigma_{i+1} \Delta x / 2 & \text{otherwise.} \end{cases} \quad (\text{B2})$$

To ensure numerical stability,  $\sigma_i$  is calculated using the van Leer limiter. After calculating the macroscopic quantities for each cell using Newtonian iteration, the distribution function  $f^{n+1}$  for the next time step is obtained. We set the calculation to converge when the criterion  $\epsilon < 10^{-10}$ .  $\epsilon$  is defined as

$$\epsilon = \sqrt{\sum_{i=1}^N (T_i^n - T_i^{n-1})^2 / N}. \quad (\text{B3})$$

For the case in Fig. 2(a), the results are shown in Tables I and II. It can be seen that in the ballistic region, the computation time of the DOM will be shorter due to the

simpler computational realization of each time step than in the DUGKS. Since the time step of the DOM needs to be smaller than the relaxation time, as the diffusion region is approached, the DOM requires a smaller cell size and time step to ensure convergence of the program, which leads to

more computational steps and increased computational time. However, for the DUGKS, the cell size and time step are not limited by the mean free path and relaxation time, resulting in excellent numerical efficiency from the ballistic to diffusive regimes.

- 
- [1] D. G. Cahill, P. V. Braun, G. Chen, D. R. Clarke, S. Fan, K. E. Goodson, P. Keblinski, W. P. King, G. D. Mahan, A. Majumdar, H. J. Maris, S. R. Phillpot, E. Pop, and L. Shi, *Appl. Phys. Rev.* **1**, 011305 (2014).
- [2] D. G. Cahill, W. K. Ford, K. E. Goodson, G. D. Mahan, A. Majumdar, H. J. Maris, R. Merlin, and S. R. Phillpot, *J. Appl. Phys.* **93**, 793 (2003).
- [3] S. J. Pearton, F. Ren, M. Tadjer, and J. Kim, *J. Appl. Phys.* **124**, 220901 (2018).
- [4] A. M. Marconnet, M. A. Panzer, and K. E. Goodson, *Rev. Mod. Phys.* **85**, 1295 (2013).
- [5] Q. Weng, S. Komiyama, L. Yang, Z. An, P. Chen, S.-A. Biehse, Y. Kajihara, and W. Lu, *Science* **360**, 775 (2018).
- [6] M.-Y. Shang, W.-H. Mao, N. Yang, B. Li, and J.-T. Lü, *Phys. Rev. B* **105**, 165423 (2022).
- [7] M.-Y. Shang, C. Zhang, Z. Guo, and J.-T. Lü, *Sci. Rep.* **10**, 8272 (2020).
- [8] A. F. Ioffe, L. S. Stil'bins, E. K. Iordanishvili, T. S. Stavitskaya, A. Gelbtuch, and G. Vineyard, *Phys. Today* **12**(5), 42 (1959).
- [9] A. Bulusu and D. G. Walker, *Superlattices Microstruct.* **44**, 1 (2008).
- [10] J. Ren, *Chin. Phys. Lett.* **40**, 090501 (2023).
- [11] L. Levitov and G. Falkovich, *Nat. Phys.* **12**, 672 (2016).
- [12] A. Aharon-Steinberg, T. Völkl, A. Kaplan, A. K. Pariari, I. Roy, T. Holder, Y. Wolf, A. Y. Meltzer, Y. Myasoedov, M. E. Huber, B. Yan, G. Falkovich, L. S. Levitov, M. Hücker, and E. Zeldov, *Nature (London)* **607**, 74 (2022).
- [13] C. Kumar, J. Birkbeck, J. A. Sulpizio, D. Perello, T. Taniguchi, K. Watanabe, O. Reuven, T. Scaffidi, A. Stern, A. K. Geim, and S. Ilani, *Nature (London)* **609**, 276 (2022).
- [14] C. R. Tellier and A. J. Tossier, *Size Effects in Thin Films* (Elsevier, Amsterdam, 1982).
- [15] G. Chen, *Nanoscale Energy Transport and Conversion: A Parallel Treatment of Electrons, Molecules, Phonons, and Photons* (Oxford University Press, New York, 2005).
- [16] J. Callaway, *Phys. Rev.* **113**, 1046 (1959).
- [17] M. Chandra, G. Kataria, D. Sahdev, and R. Sundararaman, *Phys. Rev. B* **99**, 165409 (2019).
- [18] A. Gupta, J. J. Heremans, G. Kataria, M. Chandra, S. Fallahi, G. C. Gardner, and M. J. Manfra, *Phys. Rev. Lett.* **126**, 076803 (2021).
- [19] D. A. Bandurin, I. Torre, R. K. Kumar, M. B. Shalom, A. Tomadin, A. Principi, G. H. Auton, E. Khestanova, K. S. Novoselov, I. V. Grigorieva, L. A. Ponomarenko, A. K. Geim, and M. Polini, *Science* **351**, 1055 (2016).
- [20] P. J. W. Moll, P. Kushwaha, N. Nandi, B. Schmidt, and A. P. Mackenzie, *Science* **351**, 1061 (2016).
- [21] J. Crossno, J. K. Shi, K. Wang, X. Liu, A. Harzheim, A. Lucas, S. Sachdev, P. Kim, T. Taniguchi, K. Watanabe, T. A. Ohki, and K. C. Fong, *Science* **351**, 1058 (2016).
- [22] K. Bløtekjær and E. B. Lunde, *Phys. Status Solidi B* **35**, 581 (1969).
- [23] K. Blotekjaer, *IEEE Trans. Electron. Devices* **17**, 38 (1970).
- [24] R. Stratton, *IEEE Trans. Electron. Devices* **19**, 1288 (1972).
- [25] C. Jacoboni and L. Reggiani, *Rev. Mod. Phys.* **55**, 645 (1983).
- [26] W. Miao, Y. Guo, X. Ran, and M. Wang, *Phys. Rev. B* **99**, 205433 (2019).
- [27] J. C. Chai, H. S. Lee, and S. V. Patankar, *Numer. Heat Transfer, Part B* **24**, 373 (1993).
- [28] J. C. Huang, T. Y. Hsieh, and J. Y. Yang, *J. Comput. Phys.* **290**, 112 (2015).
- [29] N. Goldsman, L. Henrickson, and J. Frey, *Solid-State Electron.* **34**, 389 (1991).
- [30] A. Gnudi, D. Ventura, and G. Baccarani, in *Proceedings of SISDEP*, edited by W. Fichtner and D. Aemmer (Hartung-Gorre, Zurich, Switzerland, 1991), Vol. 4, pp. 205–213.
- [31] K. Rahmat, J. White, and D. Antoniadis, *IEEE Trans. Comput.-Aided Des. Integr. Circuits Syst.* **15**, 1181 (1996).
- [32] K. A. Hennacy, Y. J. Wu, N. Goldsman, and I. D. Mayergoyz, *Solid-State Electron.* **38**, 1485 (1995).
- [33] K. Rupp, A. Jüngel, and T. Grasser, *J. Comput. Phys.* **229**, 8750 (2010).
- [34] Z. Guo and C. Shu, *Lattice Boltzmann Method and its Application in Engineering* (World Scientific Publishing, Singapore, 2013).
- [35] A. Chattopadhyay and A. Pattamatta, *Numer. Heat Transfer, Part B* **66**, 360 (2014).
- [36] Z. Guo, K. Xu, and R. Wang, *Phys. Rev. E* **88**, 033305 (2013).
- [37] Z. Guo, R. Wang, and K. Xu, *Phys. Rev. E* **91**, 033313 (2015).
- [38] Z. Guo and K. Xu, *Adv. Aerodyn.* **3**, 6 (2021).
- [39] C. Zhang, R. Guo, M. Lian, and J. Shiomi, *Appl. Thermal Eng.* **249**, 123379 (2024).
- [40] K. E. Nagaev and O. S. Ayyvazyan, *Phys. Rev. Lett.* **101**, 216807 (2008).
- [41] N. Hale and A. Townsend, *SIAM J. Sci. Comput.* **35**, A652 (2013).
- [42] C. Hua and A. J. Minnich, *J. Appl. Phys.* **117**, 175306 (2015).
- [43] K. Fuchs, *Math. Proc. Cambridge Philos. Soc.* **34**, 100 (1938).
- [44] E. Sondheimer, *Adv. Phys.* **1**, 1 (1952).
- [45] M. Battiato, V. Zlatić, and K. Held, *Phys. Rev. B* **95**, 235137 (2017).
- [46] P. B. Allen and M. Liu, *Phys. Rev. B* **102**, 165134 (2020).